More equable past and future warm climates in unprecedented high-resolution simulations

Jiang Zhu[1*], Bette L. Otto-Bliesner[1], Jessica E. Tierney[2],
Esther C. Brady[1], Isla R. Simpson[1], David B. Bonan[3,4], Daniel J. Lunt[5]

[1]NSF National Center for Atmospheric Research, Boulder, CO, USA.

[2]Department of Geosciences, The University of Arizona, Tucson, AZ, USA.

[3]Department of Atmospheric and Climate Science, University of Washington, WA, USA.

[4]Cooperative Institute for Climate, Ocean, and Ecosystem Studies, University of Washington, WA, USA.

[5]School of Geographical Sciences, University of Bristol, Bristol, UK.

*Corresponding author. Email: jiangzhu@ucar.edu

Understanding Earth's past warm climates is crucial for improving climate modeling and future projections. We revisit the early Eocene "Equable Climate Problem", the longstanding mismatch between proxy-inferred weak meridional and seasonal temperature contrasts at ∼50 Ma and the overly strong gradients and seasonality simulated by climate models, using the first fully coupled, high-resolution (HR) Eocene simulations. Our simulation employs ∼10× finer spatial resolution in both the atmosphere and ocean than conventional low-resolution (LR) models at ∼1–2°. The HR simulation produces a more equable Eocene climate, with over 5 °C warmer temperatures in continental interiors during winter and oceanic western boundary current regions. These temperatures more closely align with paleoclimate proxies, reducing the model-proxy discrepancy by ∼20–30% relative to LR simulations. The improvements arise from a poleward shifted

storm track with stronger wintertime atmospheric storminess at high latitudes, enhancing atmospheric heat transport and downward cloud longwave radiation, along with differences in oceanic eddy heat transport. Parallel HR simulations of future climate change similarly show additional regional and seasonal warming relative to LR. These findings indicate that traditional LR models may systematically underestimate extreme warming in past and future warm climates, underscoring the need for HR simulations in climate research and projections.

Introduction

Equable Climates refer to past warm periods—such as the Cretaceous (~100 million years ago) and the Eocene (~50 million years ago)—that have a reduced equator-to-pole temperature gradient compared to modern, and above-freezing winter temperatures at high latitudes (*1–3*). Reproducing these climates in models has historically been challenging, leading to what is known as the Equable Climate Problem (*1, 4, 5*). Recent climate models, with upgraded cloud-related parameterizations and improved paleoclimate boundary conditions, better simulate the global mean surface temperature (GMST) but still struggle to capture the high-latitude sea-surface temperature (SST) and cold month mean temperature (CMMT) (*6–9*). For example, models substantially underestimate proxy-inferred high-latitude SSTs over the Southwest Pacific and winter warmth in the continental interiors of both poles, in some cases by as much as 15–30°C (Figure 1). These persistent discrepancies imply that current models may be deficient in simulating key warm-climate processes at mid-to-high latitudes, with significant implications for predicting and preparing for future climate change, including polar amplification, hydroclimate responses, and extreme weather events (e.g. (*10, 11*)).

Here we revisit the “Equable Climate Problem” of the early Eocene by conducting, to the best of our knowledge, the first fully coupled paleoclimate simulation at an unprecedented horizontal resolution in both the atmosphere and ocean—approximately 10× finer than that of traditional low-resolution (LR) models at 1–2° (Materials and Methods). This advancement is made possible by recent progress in high-resolution (HR) modeling and supercomputing capabilities. A key advantage of HR models (at a grid spacing of ~10 km in the ocean and ~ 25 km in the atmosphere) is that they explicitly resolve, rather than parameterize, ocean eddies, and they improve the representation of mesoscale air-sea interactions and mesoscale weather features in the atmosphere (*12–14*). As a result, a wide range of atmospheric, hydroclimate, and oceanic processes are simulated more realistically (*12–19*). Despite these advantages, HR capabilities have rarely been applied in paleoclimate contexts, due both to their high computational cost (typically ∼100× that of LR models) and the substantially different boundary conditions and long integrations required for ocean-atmosphere coupled paleoclimate simulations to approach equilibrium. We address these challenges with a new spin-up strategy: first running a corresponding LR paleoclimate simulation for several thousand years to achieve near equilibrium, then interpolating its ocean state to initialize the HR run (Materials and Methods). This approach enables us to conduct the HR simulation for 60 model years, allowing direct comparison with its LR counterpart and providing insights into the climatic impact of resolution at decadal and potentially longer timescales.

Results

Deficiencies in modeled temperatures in the low-resolution simulation

The LR simulation was run with the Community Earth System Model version 1.3 (CESM1.3), using a similar setup to the previously published CESM1.2 simulations (Materials and Methods) (*6, 20*). The Eocene GMST in the new LR CESM1.3 simulation matches that in CESM1.2 (24.9 °C, calculated using 2-meter air temperature). Similar to CESM1.2, CESM1.3 reproduces 21 out of 53 Eocene proxy records of the mean annual air temperature (MAAT) within their uncertainty (90% confidence intervals; CI), and 14 out of 29 proxy SST records (Figure 1A-C). The overall root-mean-square errors (RMSEs) of simulating the proxy MAAT and SST are 7.3 °C and 7.8 °C respectively, both comparable to the averaged intrinsic proxy uncertainties (>5–6 °C; 90% CI; Supplementary Materials Data S1 and S2), especially given the methodological differences among reconstructions (*21–24*). The equator-to-pole SST gradient is similar in CESM1.2 and CESM1.3, both falling within the proxy-suggested ∼28% (90% CI of 14–46%) reduced SST gradient (with the deep-ocean temperature used as a substitute for the polar SSTs due to proxy scarcity) (*9*).

The model–data mismatch is much larger for winter temperatures, particularly for continental interior high-Arctic sites (Figures 1B,2B). Across sites, the RMSE increases to 9.8 °C for CMMT, with the greatest errors occurring inland. For example, at the Giraffe Kimberlite site in the Canadian Arctic, proxies indicate a CMMT of 3.4 °C from mutual climate range analysis, a warm winter condition further supported by palm phytoliths and warm-water aquatic organisms (*25, 26*). In contrast, the LR simulation produces extremely cold winters with a CMMT near -18 °C. Likewise, for the New Siberian Islands in Russia, proxy data suggest CMMTs of about 11 °C based on warm-winter fossil taxa (*27*), while the model simulates -19 °C. These interior Arctic sites provide strong constraints on minimum winter temperatures due to their inland setting and well-preserved proxy records. For the non-Arctic sites (paleolatitude $< 60°$), the RMSE in CMMT is substantially lower, at 8.0°C compared with 15.0°C for the Arctic.

The LR simulation also substantially underestimates the warm SSTs observed in the Southwest Pacific near New Zealand, where multiple proxy records indicate temperatures of ~30 °C (Figures 1C,2C). In contrast, the model simulates SSTs of only ~15 °C in this region under 3× preindustrial CO_2, yielding a discrepancy of ~15 °C. This pronounced model–data mismatch in the Southwest Pacific stands in contrast to other regions, where LR reproduces regional SSTs more accurately. For instance, the model simulates a tropical mean SST of 33.0 °C, matching proxy reconstructions within their uncertainty (35.0 ± 3.7 °C; 90% CI).

Importantly, the model–data mismatches in both high-latitude winter temperatures and Southwest Pacific SSTs are not unique to CESM1 but are common across all models participating in the Deep-Time Model Intercomparison Project (DeepMIP), highlighting a persistent and unresolved challenge in simulating key aspects of the Eocene climate (*7–9, 28*). Together, these results suggest that the discrepancies likely stem from missing or inadequate representation of model physics, or the absence of additional, non-traditional forcings that are typically excluded from current climate models (*4, 10, 29–32*). Nevertheless, uncertainties in proxy interpretations and calibrations cannot be fully ruled out (*22, 28, 33*).

Improved and more equable climate in the high-resolution simulation

The HR simulation produces a markedly more equable climate than the LR, with both reduced spatial temperature contrasts and reduced seasonal variations. Winters are substantially warmer in the HR simulation, with CMMTs exceeding those in the LR simulation across the continental interiors of both polar regions (Figure 1E,G). At both the Giraffe Kimberlite and the New Siberian

Islands sites, CMMTs in HR are approximately 5 °C higher than in LR, reducing model bias by up to ~25%. In contrast, temperature differences for low-latitude land and annual means remain modest, generally less than 1–2 °C at most locations (Figures 1D and 2A). Aggregating all high-Arctic proxy sites, the HR simulation reduces the RMSE in CMMT by about 2 °C compared to LR (from 15.1 to 13.1 °C) and reduces the RMSE for MAAT from 9.3 to 8.3 °C. The increased winter warmth over continental interiors is linked to a reduction in temperature seasonality (Figure 3A,C). Over the Canadian Arctic (land area between 50–75°N and 100–40°W), LR simulates a seasonal temperature amplitude of ~41 °C (T_{season}, defined as the temperature difference between the warmest and coldest months in the climatology), while HR exhibits a smaller amplitude of ~37 °C, corresponding to a 10% reduction (Figure 3B). Similarly, seasonality over Siberia (land area between 58–75°N and 75–105°E) declines by approximately 10% (~4 °C, Figure 3D). These simulated Eocene seasonal temperature ranges are considerably narrower than those in present-day climate, which reaches 55 °C over Siberia and 45 °C over the Canadian Arctic (*34*).

The HR simulation demonstrates notably warmer SSTs as well, particularly in mid-to-high latitudes (Figures 1F,H and 2C). In the Southwest Pacific region, SSTs are up to 5 °C warmer than in the LR simulation, reducing the model bias by ~30%. Similarly elevated SSTs are found over other western boundary current systems, including the Northwest Pacific, Northwest Atlantic, and Southwest Atlantic. While SSTs in low-latitude regions are also higher in HR, the average difference is smaller, at approximately 1 °C. The enhanced SST warming over western boundary current regions in our coupled simulations qualitatively agrees with results from previous ocean-only simulations of past warm climates (*35*).

CESM1 LR is one of the best-performing DeepMIP models for the early Eocene, simulating global mean temperature, precipitation, oxygen isotopes, and inferred vegetation distribution in good agreement with proxy records (*7, 9, 36–38*). CESM1 HR further enhances the simulation of regional and seasonal temperatures, reducing model-data discrepancies by ~20–30%. Apart from minor tuning adjustments to maintain top-of-atmosphere radiation balance (*13*), HR and LR share nearly identical boundary and initial conditions and differ primarily in horizontal resolution (Materials and Methods). The enhanced performance of the HR simulation can therefore be attributed largely to its finer horizontal resolution. We further suggest that the improvements in HR identified here would persist if substantially greater computational resources were available to extend the simulation beyond 60 years, as both the GMST and top-of-model radiation are relatively stable in HR and are not very different from the LR counterparts (Figure S1). Together with the underlying physical mechanisms, which operate on relatively short timescales (see next section), this supports the robustness of the HR improvements beyond decadal timescales.

Mechanisms for the More Equable Climate at High Resolution

To identify the mechanisms underlying the more equable and realistic climate in the HR simulation, we first disentangle the relative contributions of atmospheric and oceanic horizontal resolution, given that both components are refined in the fully coupled HR configuration. To this end, we analyze an additional hybrid-resolution simulation (HaLo; *H*igh-resolution *a*tmosphere and *L*ow-resolution *o*cean), in which the atmosphere and land components employ the same horizontal resolution as the HR simulation and the ocean and sea ice remain at the same resolution as in the LR simulation (Materials and Methods). Comparisons between HaLo and LR therefore primarily isolate the effects of increased atmospheric resolution, whereas differences between HR and HaLo quantify the contribution of enhanced oceanic resolution. Because additional pathways may operate in the coupled system—for example, changes in ocean resolution can modify SST patterns and thereby influence land temperatures via SST-mediated atmospheric responses—we also conduct atmosphere-only simulations with prescribed SSTs to isolate the role of these SST-mediated atmospheric pathways (Materials and Methods).

As shown in Figures 4A and B, HaLo exhibits up to 5 °C of continental winter warming relative to LR, while HR produces a smaller winter warming of ~1–2 °C relative to HaLo, largely confined to coastal regions. Resolution-induced differences in land temperature are strongly seasonally asymmetric, peaking in winter and remaining negligible in summer. As a result, CMMT increases by approximately 4 °C on average over the Canadian Arctic and Siberia regions (Figures 3A,C). Higher atmospheric resolution accounts for more than half of the reduction in the seasonal temperature range between HR and LR (ΔT_{season}). This interpretation is supported by the pronounced decrease in ΔT_{season} of ~3 °C between HaLo and LR, two fully coupled simulations that differ only in atmospheric resolution (Figures 3B,D). Further support comes from the substantial reduction in ΔT_{season} of ~2 °C in HaLo relative to an additional LR atmosphere-only simulation forced with HaLo SSTs ($\mathrm{La\_SST_{HaLo}}$; Materials and Methods). Because HaLo and $\mathrm{La\_SST_{HaLo}}$ share identical

SST climatology but differ in atmospheric resolution, this comparison isolates the direct influence of atmospheric resolution, independent of SST-mediated feedbacks. In contrast, changes in ocean resolution exert only a minor influence on $\Delta T_{\mathrm{season}}$ when atmospheric resolution is held fixed. Specifically, $\Delta T_{\mathrm{season}}$ differs by less than 1 °C between HR and HaLo (two coupled simulations with identical high-resolution atmosphere but different ocean resolution) and between $\mathrm{La\_SST_{HR}}$ and $\mathrm{La\_SST_{LR}}$, which employ the same low-resolution atmosphere but prescribe SSTs from HR and LR, respectively (Materials and Methods). Overall, atmospheric resolution emerges as the primary driver of enhanced continental winter warming and reduced seasonality in the HR configuration.

We hypothesize that the improved representation of synoptic- and mesoscale atmospheric systems in the HR simulation enhances diabatic heating, storm activity, and cloudiness at high latitudes, leading to warmer winters in continental interiors. Consistent with this interpretation, wintertime storminess, quantified by 2–8-day bandpass-filtered eddy kinetic energy at 850 hPa ($\mathrm{EKE_{850}}$; Materials and Methods), is approximately 30% greater in HR than in the LR simulation at high latitudes in association with a more poleward shifted stormtrack (Figure 5). This enhanced high-latitude storminess is accompanied by stronger meridional eddy heat flux, increased cloud cover and cloud water content and associated increases in downward longwave radiation, and greater precipitation (Figure S2). The increases in cloudiness and their longwave radiative effects are consistent with previous studies linking enhanced low clouds to polar winter warming as a potential contributor to resolving the Equable Climate Problem (*10*). The enhanced high-latitude storminess is associated with a poleward shift of wintertime storm tracks in both preindustrial and Eocene HR simulations, with a markedly stronger signal under Eocene warming (Figure S3). This behavior is consistent with theoretical and modeling studies highlighting the role of latent heating in modulating high-latitude storminess (*39–42*), as well as with the poleward shift of storm tracks seen in high-resolution models (*43–45*). It also aligns with earlier work demonstrating that higher atmospheric resolution is required to resolve the mesoscale structure of winter storms, their associated latent heating, and their interactions with jet streams without excessive numerical diffusion (*45–47*). Importantly, the resolution-driven enhancement and poleward shift of storminess are primarily attributable to increased atmospheric resolution, supporting our proposed mechanism, whereas higher oceanic resolution mainly contributes to weaker storminess over much of the mid-latitude oceans (Figures 5C,D).

In contrast to atmospheric resolution, higher oceanic resolution explains the warmer SSTs across mid-latitude western boundary current regions and provides a secondary contribution to continental warming. Regions of pronounced SST warming coincide with areas of intense oceanic eddy activity (Figures 4 and S4; Materials and Methods), indicating that explicitly resolved eddies in HR influence ocean temperatures in ways not fully captured by the parameterized eddies in LR. Enhanced ocean resolution with resolved eddies tends to cool tropical SSTs while warming mid-latitude SSTs (HR versus HaLo in Figure 4D; see also Figure S5F for the parallel preindustrial simulations), consistent with stronger eddy-induced meridional heat transport. Additional warming likely arises from reduced vertical heat redistribution in high-resolution ocean with explicit simulation of mesoscale ocean eddies (*17*). These results reinforce the importance of explicitly resolving oceanic mesoscale eddies for regional SSTs and point to potential deficiencies in current-generation eddy parameterizations (*12, 13, 17, 48, 49*). For example, a recent study introduced a stochastic energetics-based scheme into an ocean eddy parameterization to represent missing eddy-induced variability in LR and found enhanced meridional heat transport in eddy-rich western boundary current regions and the Antarctic Circumpolar Current, leading to warmer SSTs (*50*).

We emphasize that the benefits of high resolution in paleoclimate simulations stem from its improved representation of the modern climate, and we further suggest that these resolution-related improvements are state dependent and become more pronounced under strong external forcing. Consistent with this interpretation, the HR configuration performs better in present-day simulations, yielding more realistic winter temperatures over continental interiors and more accurate SST structures along western boundary currents (Figures S6, S5; see also (*12, 13*)). For example, relative to reanalysis (averaged over 1950–1978), the LR preindustrial simulation exhibits a cold bias in CMMT exceeding 5 °C across much of the high Arctic, particularly over Siberia, whereas HR substantially reduces the spatial extent of this bias, primarily due to the increased atmospheric resolution (Figures S6D,F,H). Consistently, enhanced ocean resolution reduces SST biases over the western boundary current regions when compared with present-day observation (Figure S5). Beyond mean-state temperatures, HR more accurately captures climate variability over western boundary current regions (*18*), better reproduces observed ocean heat uptake during the historical period (see Figure 1 of (*17*)), and demonstrates higher predictive skill in decadal forecast systems (*16*). Importantly, we note that the structural differences identified in our relatively short (60-year) Eocene

HR simulation closely resemble those found in the long preindustrial HR simulation exceeding 700 years, indicating that our results are robust and unlikely to be strongly influenced by the limited length of the HR simulations.

Under Eocene warming, these resolution-related differences intensify, indicating a clear state-dependent resolution effect. In particular, diabatic heating and storminess associated with finer atmospheric resolution strengthens as temperatures rise, consistent with the nonlinear Clausius–Clapeyron relationship (Figure S3). Likewise, oceanic processes may also establish a positive feedback that enhances the impact of resolution under strong external forcing. Specifically, HR models tend to simulate a more stratified and realistic upper ocean in the background state, which leads to reduced ocean heat uptake below 250 m and a warmer upper ocean layer compared to LR counterparts for comparable surface fluxes (*17*). Together, these mechanisms amplify the climatic influence of resolution when external forcing is strong.

Implications for modern-day climate change

To evaluate the implications of our findings for modern-day climate change, we performed parallel HR and LR simulations with present-day continental configurations under 4×CO_2 forcing. The LR 4×CO_2 experiment was branched from a preindustrial (PI) simulation and integrated for 2,700 model years. The HR simulation was then initialized and integrated for 50 years, following the same initialization procedure used for the HR Eocene experiment (Materials and Methods). This pair of quasi-equilibrated 4×CO_2 simulations isolates the influence of model resolution on equilibrated warm climate states and enables direct comparison with the Eocene results. To further assess resolution effects under more moderate warming, we analyzed 10-member ensembles of HR and LR Representative Concentration Pathway 8.5 (RCP8.5) simulations from the Understanding the Role of MESoscale Atmosphere–Ocean Interactions in Seasonal-to-Decadal CLImate Prediction (MESACLIP) project (*13, 19, 51, 52*). These transient experiments complement the 4×CO_2 and Eocene simulations by sampling resolution-driven differences in a transient 21st-century emissions scenario. The 10-member ensemble also reduces much of the influence of internal variability on our results.

Consistent with the Eocene experiments, both the HR 4×CO_2 and RCP8.5 simulations exhibit substantially warmer CMMT over high latitudes than its LR counterpart (Figure 6), with differences reaching up to 5 °C over Siberia and the Canadian Arctic. At the process level, these simulations show a poleward shift and intensification of storminess along the poleward flanks, accompanied by increases in cloudiness and associated cloud radiative effects, closely mirroring the behavior seen in the Eocene simulations (Figure S3). Both HR simulations also produce enhanced warming along western boundary current regions, consistent with the Eocene results, albeit with reduced magnitude. The similarity of these responses across climate states highlights the broader relevance of the resolution-dependent mechanisms identified here for future climate projections. In particular, enhanced diabatic heating and ocean eddy–driven heat transport and redistribution operate in a comparable manner in PI-based future warming experiments as atmospheric and oceanic resolution increase. Nonetheless, differences in background states between the Eocene and the modern world may modulate the strength and expression of these effects through factors such as distinct continental configurations, cryospheric feedbacks, and altered freshwater and heat exchange through ocean gateways (*53*).

Building on our Eocene results, we propose that CMMT differences between HR and LR simulations become increasingly pronounced in warmer climates because the mesoscale latent-heating feedback is state dependent, intensifying with temperature through the nonlinear Clausius–Clapeyron relationship. The resulting enhancement of winter warming and storminess implies reduced cold extremes, such as cold-air outbreaks, particularly over continental interiors, where winter storms already cause multi-billion-dollar damages in regions such as the continental United States.

Discussion

We have investigated how unprecedented high horizontal resolution influences simulated temperatures in early Eocene and future warming simulations. We find that the high-resolution Eocene simulation produces up to 5 °C warmer temperatures in high-latitude continental interiors during winter and in western boundary current regions, yielding a more equable climate with reduced spatial and seasonal temperature gradients. Similar enhancements in surface temperature responses are also evident in parallel high-resolution simulations of future warming. These results suggest that key characteristics of both past and future climate change—including polar amplification, regional and seasonal temperature patterns, and associated hydrological and extreme-event responses, may be underestimated or incompletely represented in conventional low-resolution models. Our findings are consistent with a growing body of literature highlighting the limitations of low-resolution models and the benefits of increased resolution (*18, 19, 53*), while providing a long-term climate change and paleoclimate perspective.

High resolution helps to address the long-standing "Equable Climate Problem" by reducing the model-proxy discrepancies by up to 30%. Nevertheless, at $3\times CO_2$, substantial model-proxy mismatches persist, indicating that the high resolution employed in this study alone is insufficient to fully reconcile models with proxy evidence. One contributing factor is that our HR Eocene simulation adopts 3× preindustrial CO_2, which lies at the lower end of recent reconstructions (*54, 55*), and model–proxy agreement would therefore be expected to improve under stronger CO_2 forcing. The remaining discrepancies likely reflect a combination of factors, including the need for even finer resolution, additional feedback mechanisms, and uncertainties in proxy reconstructions and paleoclimate boundary conditions. As an illustrative example, if high-latitude SST proxies are assumed to reflect local summer temperatures—consistent with a light limitation on biological growth—RMSE in the HR simulation decreases to 5.3 °C and approaches the intrinsic mean proxy uncertainty, compared with 6.6 °C for the annual-mean SST (Figure 2C). We suggest that future progress will likely depend on improved constraints on CO_2 and non-CO_2 boundary conditions (e.g., paleogeography, vegetation, and land surface properties), together with continued advances in model resolution, physical fidelity, and proxy reconstruction techniques. Despite these remaining uncertainties, the HR simulations reported here represent significant progress relative to traditional low-resolution models.

Our results underscore the critical role of increasing model resolution for simulating both past and future warm climates. Higher resolution enhances the representation of weather and climate systems, primarily through better resolving synoptic- and mesoscale atmospheric activities and more accurate depiction of oceanic eddies. While the current HR simulations still depend on several parameterizations, further gains may be achieved by moving toward kilometer-scale, storm-resolving models that explicitly capture deep convection and a broader spectrum of mesoscale and submesoscale processes.

We encourage the climate dynamics and paleoclimate communities to adopt high-resolution modeling capabilities early and to pursue innovative strategies for assessing their influence on both past and future warm climates, particularly regarding hydrological cycle changes and extreme events. High resolution is especially valuable for paleoclimate studies, as many proxy records originate from coastal and eddy-rich regions with high biological productivity and strong spatial heterogeneity. A hierarchical modeling framework that combines high- and standard-resolution configurations, leveraging the physical realism of the former together with the long, fully equilibrated spinups of the latter, is essential for delivering more robust climate representations.

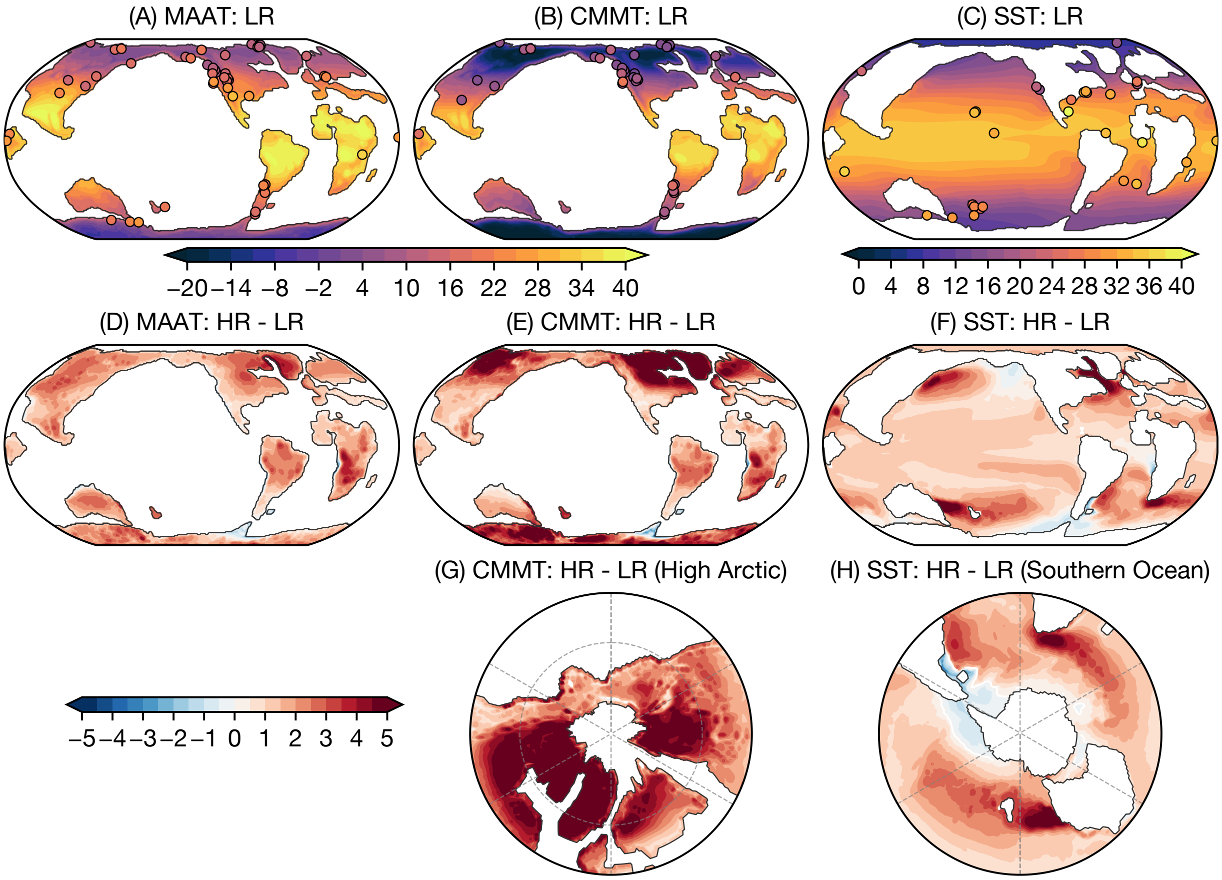

Figure 1: **Spatial distribution, model–data comparison, and resolution dependence of Eocene temperatures (°C).** (**A**) Mean annual surface air temperature (MAAT) from the low-resolution (LR) simulation (shading) compared with proxy reconstructions (markers). (**B**, **C**) Same as **A**, but for cold-month mean temperature (CMMT) and annual mean sea-surface temperature (SST), respectively. (**D**) Difference in MAAT between the high-resolution (HR) and LR simulations. (**E**, **F**) As in **D**, but for CMMT and SST, respectively. (**G**, **H**) As in **E** and **F**, but shown in a polar projection to highlight resolution-induced differences at high latitudes.

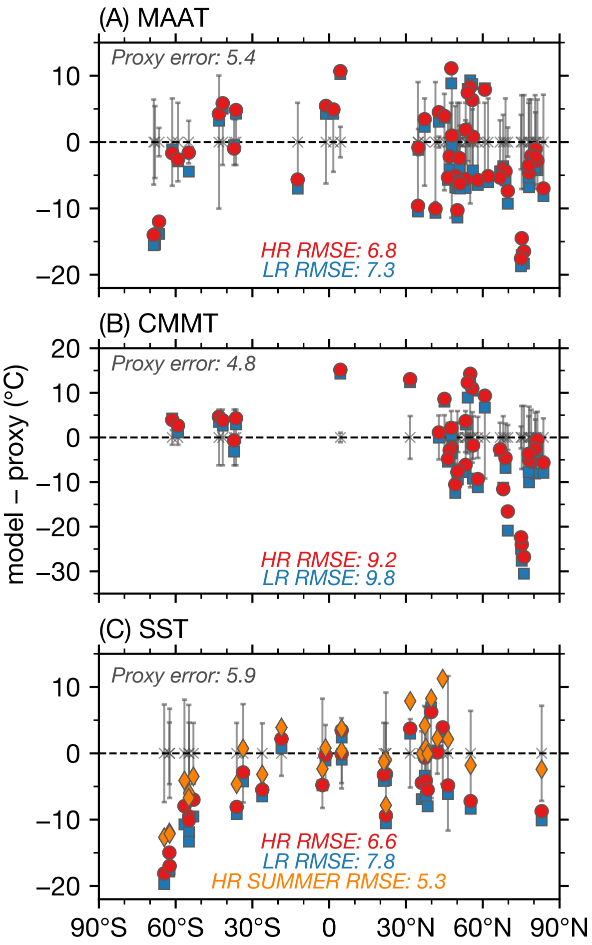

Figure 2: **Model–data comparison of Eocene temperatures and resolution dependence.** (**A**) Latitudinal distribution of model–proxy differences in mean annual surface air temperature (MAAT) from the low-resolution (LR; blue) and high-resolution (HR; red) simulations. (**B**, **C**) As in **A**, but for cold-month mean temperature (CMMT) and sea-surface temperature (SST), respectively. In **C**, model–data comparisons of summer-mean SST are also shown (orange), assuming the proxies reflect summer SSTs; summer is defined as the warmest consecutive three months. Error bars indicate the 90% confidence intervals of proxy uncertainties. Colored numbers denote the root-mean-square errors (RMSE) across all available proxy sites.

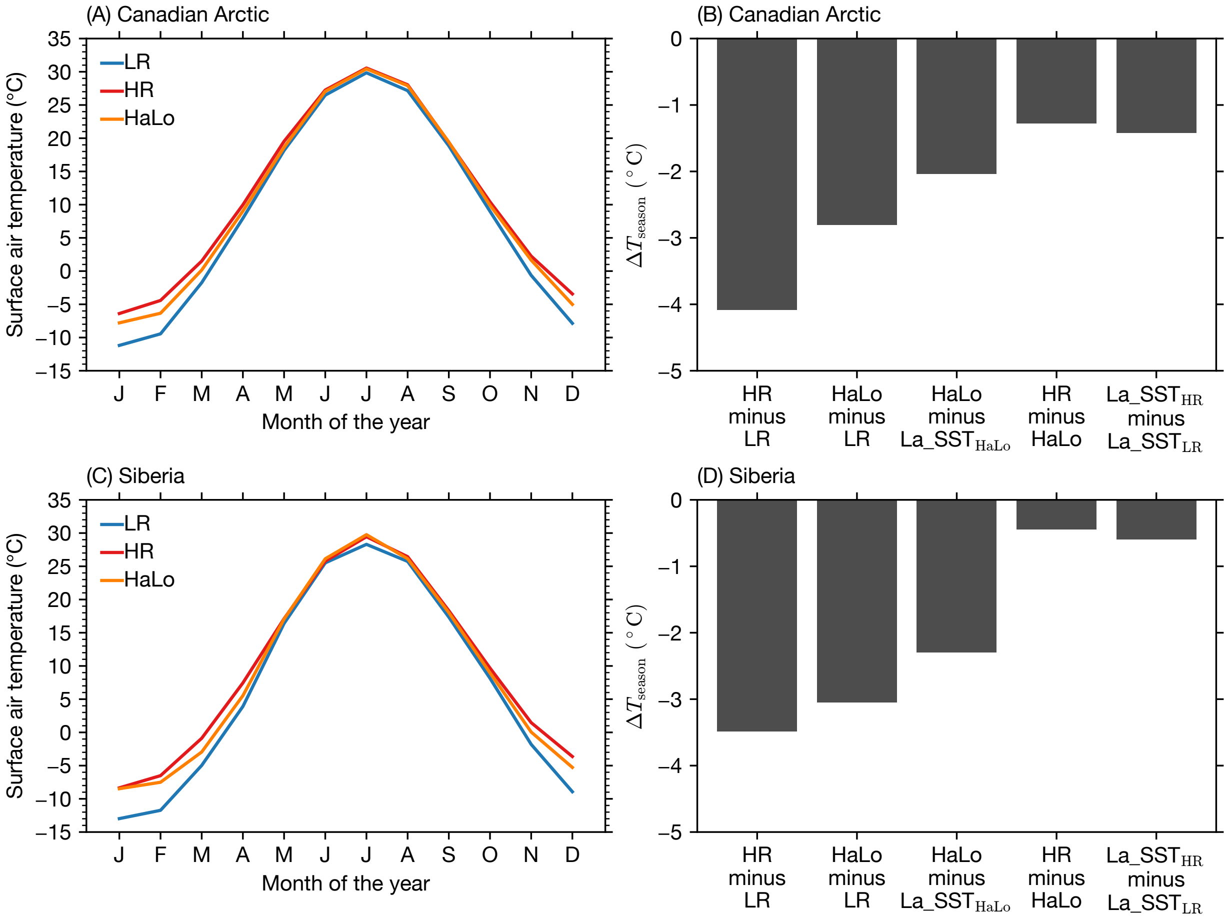

Figure 3: **Seasonal temperature range over the high Arctic across different simulations.** (**A**) Climatological surface air temperature (SAT) by month of the year in the low-resolution (LR), high-resolution (HR), and hybrid high-resolution–atmosphere/low-resolution–ocean (HaLo) simulations, averaged over land in the Canadian Arctic (50–75°N, 100–40°W). (**B**) Differences in the seasonal SAT range ($\Delta T_{\mathrm{season}}$) over the Canadian Arctic among the HR, LR, HaLo, and atmosphere-only simulations with prescribed sea-surface temperatures (SSTs) from HR (La_SST$_{\mathrm{HR}}$), LR (La_SST$_{\mathrm{LR}}$), and HaLo (La_SST$_{\mathrm{HaLo}}$), respectively. (**C**, **D**) Same as **A** and **B**, but for Siberia (58–75°N, 75–105°E).

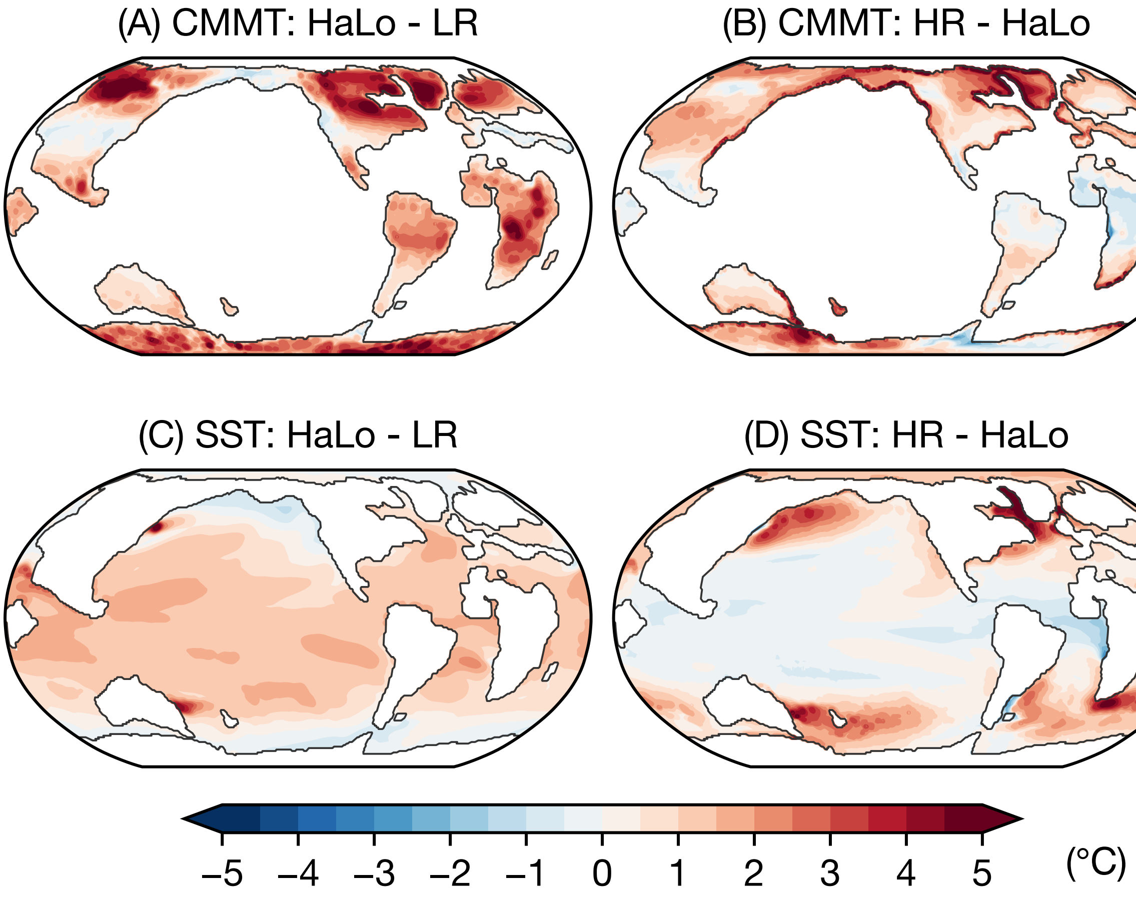

Figure 4: **Effects of model resolution on simulated temperatures isolated by a hybrid-resolution simulation.** (**A**) Difference in cold-month mean temperature (CMMT) between the hybrid high-resolution–atmosphere/low-resolution–ocean (HaLo) and low-resolution (LR) simulations. (**B**) Same as **A**, but showing the difference between the high-resolution (HR) and HaLo simulations. (**C**, **D**) Same as **A** and **B**, respectively, but for annual-mean sea-surface temperature (SST).

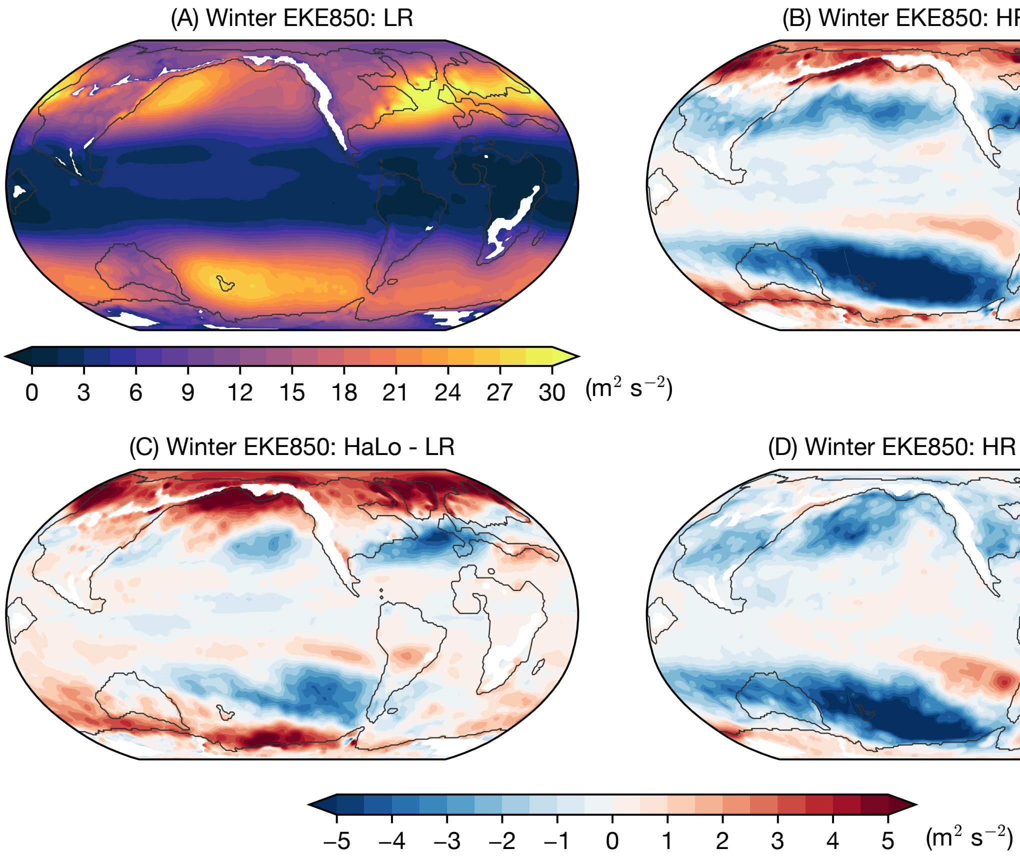

Figure 5: **Resolution dependence of wintertime storminess.** (**A**) Storminess, quantified by eddy kinetic energy at 850 hPa (EKE$_{850}$), in the low-resolution (LR) simulation. (**B**) Difference in EKE$_{850}$ between the high-resolution (HR) and LR simulations. (**C**) Same as **B**, but showing the difference between the hybrid high-resolution–atmosphere/low-resolution–ocean (HaLo) and LR simulations. (**D**) Same as **B**, but showing the difference between the HR and HaLo simulations. Winter is defined as December–February (DJF) for the Northern Hemisphere and June–August (JJA) for the Southern Hemisphere. EKE$_{850}$ is calculated using bandpass-filtered daily data.

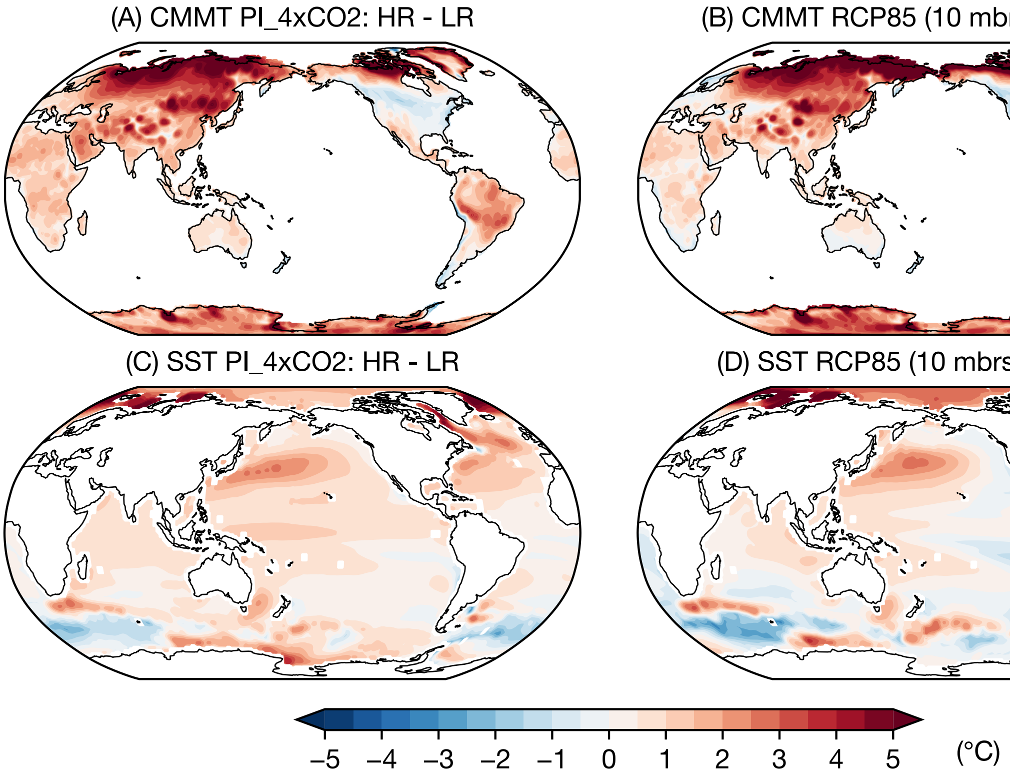

Figure 6: **High-resolution simulations produce warmer winters and western boundary current regions under future climate forcing.** (**A**) Difference in cold-month mean temperature (CMMT) between the high-resolution (HR) and low-resolution (LR) simulations for the abrupt 4×CO_2 experiment. (**B**) Same as **A**, but for the RCP8.5 simulations. Shown are ensemble means from ten RCP8.5 members averaged between 2071 and 2100. (**C, D**) Same as **A** and **B**, but for the annual mean sea surface temperature (SST).

References and Notes

1. E. J. Barron, Eocene Equator-to-pole Surface Ocean Temperatures: A Significant Climate Problem? *Paleoceanography* **2** (6), 729–739 (1987), doi:10.1029/PA002i006p00729.

2. D. R. Greenwood, S. L. Wing, Eocene Continental Climates and Latitudinal Temperature Gradients. *Geology* **23** (11), 1044–1048 (1995), doi:10.1130/0091-7613(1995)023⟨1044:ECCALT⟩2.3.CO;2.

3. J. E. Tierney, J. S. Sinninghe Damste, R. D. Pancost, A. Sluijs, J. C. Zachos, Eocene Temperature Gradients. *Nature Geosci* **10** (8), 538–539 (2017).

4. M. Huber, R. Caballero, The Early Eocene Equable Climate Problem Revisited. *Climate of the Past* **7** (2), 603–633 (2011), doi:10.5194/cp-7-603-2011.

5. D. J. Lunt, *et al.*, A Model–Data Comparison for a Multi-Model Ensemble of Early Eocene Atmosphere–Ocean Simulations: EoMIP. *Climate of the Past* **8** (5), 1717–1736 (2012), doi:10.5194/cp-8-1717-2012.

6. J. Zhu, C. J. Poulsen, J. E. Tierney, Simulation of Eocene Extreme Warmth and High Climate Sensitivity through Cloud Feedbacks. *Science Advances* **5** (9), eaax1874 (2019), doi:10.1126/sciadv.aax1874.

7. D. J. Lunt, *et al.*, DeepMIP: Model Intercomparison of Early Eocene Climatic Optimum (EECO) Large-Scale Climate Features and Comparison with Proxy Data. *Clim. Past* **17** (1), 203–227 (2021), doi:10.5194/cp-17-203-2021.

8. I. Niezgodzki, *et al.*, Simulation of Arctic Sea Ice within the DeepMIP Eocene Ensemble: Thresholds, Seasonality and Factors Controlling Sea Ice Development. *Global and Planetary Change* **214**, 103848 (2022), doi:10.1016/j.gloplacha.2022.103848.

9. J. Zhu, C. J. Poulsen, B. L. Otto-Bliesner, Modeling Past Hothouse Climates as a Means for Assessing Earth System Models and Improving the Understanding of Warm Climates. *Annual Review of Earth and Planetary Sciences* **52**, 351–78 (2024), doi:10.1146/annurev-earth-032320-100333.

10. T. W. Cronin, E. Tziperman, Low Clouds Suppress Arctic Air Formation and Amplify High-Latitude Continental Winter Warming. *Proceedings of the National Academy of Sciences* **112** (37), 11490 LP – 11495 (2015), doi:10.1073/pnas.1510937112.

11. K. Hartig, E. Tziperman, Suppression of Cold Air Outbreaks over the Interior of North America in a Warmer Climate. *Journal of Climate* **37** (17), 4541–4557 (2024), doi: 10.1175/JCLI-D-23-0477.1.

12. R. J. Small, *et al.*, A New Synoptic Scale Resolving Global Climate Simulation Using the Community Earth System Model. *Journal of Advances in Modeling Earth Systems* **6** (4), 1065–1094 (2014), doi:10.1002/2014MS000363.

13. P. Chang, *et al.*, An Unprecedented Set of High-Resolution Earth System Simulations for Understanding Multiscale Interactions in Climate Variability and Change. *Journal of Advances in Modeling Earth Systems* **12** (12), e2020MS002298 (2020), doi:10.1029/2020MS002298.

14. M. J. Roberts, *et al.*, High-Resolution Model Intercomparison Project Phase 2 (HighResMIP2) towards CMIP7. *Geosci. Model Dev.* **18** (4), 1307–1332 (2025), doi:10.5194/gmd-18-1307-2025.

15. A. Czaja, C. Frankignoul, S. Minobe, B. Vannière, Simulating the Midlatitude Atmospheric Circulation: What Might We Gain From High-Resolution Modeling of Air-Sea Interactions? *Current Climate Change Reports* **5** (4), 390–406 (2019), doi:10.1007/s40641-019-00148-5.

16. S. G. Yeager, *et al.*, Reduced Southern Ocean Warming Enhances Global Skill and Signal-to-Noise in an Eddy-Resolving Decadal Prediction System. *npj Climate and Atmospheric Science* **6** (1), 107 (2023), doi:10.1038/s41612-023-00434-y.

17. G. Xu, *et al.*, Enhanced Upper Ocean Warming Projected by the Eddy-Resolving Community Earth System Model. *Geophysical Research Letters* **50** (21), e2023GL106100 (2023), doi: 10.1029/2023GL106100.

18. J. G. Larson, D. W. J. Thompson, J. W. Hurrell, Signature of the Western Boundary Currents in Local Climate Variability. *Nature* **634** (8035), 862–867 (2024), doi:10.1038/s41586-024-08019-2.

19. P. Chang, *et al.*, Future Extreme Precipitation Amplified by Intensified Mesoscale Moisture Convergence. *Nature Geoscience* (2025), doi:10.1038/s41561-025-01859-1.

20. J. E. Tierney, *et al.*, Spatial Patterns of Climate Change across the Paleocene–Eocene Thermal Maximum. *Proceedings of the National Academy of Sciences* **119** (42), e2205326119 (2022), doi:10.1073/pnas.2205326119.

21. C. J. Hollis, *et al.*, The DeepMIP Contribution to PMIP4: Methodologies for Selection, Compilation and Analysis of Latest Paleocene and Early Eocene Climate Proxy Data, Incorporating Version 0.1 of the DeepMIP Database. *Geoscientific Model Development* **12** (7), 3149–3206 (2019), doi:10.5194/gmd-12-3149-2019.

22. G. N. Inglis, J. E. Tierney, *The TEX86 Paleotemperature Proxy*, Elements in Geochemical Tracers in Earth System Science (Cambridge University Press, Cambridge) (2020), doi:10.1017/9781108846998.

23. T. Reichgelt, *et al.*, Plant Proxy Evidence for High Rainfall and Productivity in the Eocene of Australia. *Paleoceanography and Paleoclimatology* **n/a** (n/a), e2022PA004418 (2022), doi:10.1029/2022PA004418.

24. G. N. Inglis, *et al.*, Surface Ocean Cooling in the Eocene North Atlantic Coincides With Declining Atmospheric CO2. *Geophysical Research Letters* **50** (24), e2023GL105448 (2023), doi:10.1029/2023GL105448.

25. A. P. Wolfe, *et al.*, Middle Eocene CO2 and Climate Reconstructed from the Sediment Fill of a Subarctic Kimberlite Maar. *Geology* **45** (7), 619–622 (2017), doi:10.1130/G39002.1.

26. P. A. Siver, A. V. Reyes, A. Pisera, S. D. Buryak, A. P. Wolfe, Palm Phytoliths in Subarctic Canada Imply Ice-Free Winters 48 Million Years Ago during the Late Early Eocene. *Annals of Botany* p. mcaf021 (2025), doi:10.1093/aob/mcaf021.

27. G. Suan, *et al.*, Subtropical Climate Conditions and Mangrove Growth in Arctic Siberia during the Early Eocene. *Geology* **45** (6), 539–542 (2017), doi:10.1130/G38547.1.

28. D. J. Lunt, *et al.*, Paleoclimate Data Provide Constraints on Climate Models' Large-Scale Response to Past CO2 Changes. *Communications Earth & Environment* **5** (1), 419 (2024), doi:10.1038/s43247-024-01531-3.

29. K. Emanuel, A Simple Model of Multiple Climate Regimes. *Journal of Geophysical Research: Atmospheres* **107** (D9), ACL 4–1 (2002), doi:10.1029/2001JD001002.

30. R. L. Sriver, M. Huber, Observational Evidence for an Ocean Heat Pump Induced by Tropical Cyclones. *Nature* **447** (7144), 577–580 (2007), doi:10.1038/nature05785.

31. D. S. Abbot, E. Tziperman, Sea Ice, High-Latitude Convection, and Equable Climates. *Geophysical Research Letters* **35** (3), L03702 (2008), doi:10.1029/2007GL032286.

32. D. Dutta, *et al.*, Early Eocene Low Orography and High Methane Enhance Arctic Warming via Polar Stratospheric Clouds. *Nature Geoscience* **16** (11), 1027–1032 (2023), doi:10.1038/s41561-023-01298-w.

33. C. J. Hollis, *et al.*, Early Paleogene Temperature History of the Southwest Pacific Ocean: Reconciling Proxies and Models. *Earth and Planetary Science Letters* **349–350**, 53–66 (2012), doi:10.1016/j.epsl.2012.06.024.

34. H. Hersbach, *et al.*, The ERA5 Global Reanalysis. *Quarterly Journal of the Royal Meteorological Society* **146** (730), 1999–2049 (2020), doi:10.1002/qj.3803.

35. P. D. Nooteboom, *et al.*, Improved Model-Data Agreement With Strongly Eddying Ocean Simulations in the Middle-Late Eocene. *Paleoceanography and Paleoclimatology* **37** (8), e2021PA004405 (2022), doi:10.1029/2021PA004405.

36. J. Zhu, *et al.*, Simulation of Early Eocene Water Isotopes Using an Earth System Model and Its Implication for Past Climate Reconstruction. *Earth and Planetary Science Letters* **537**, 116164 (2020), doi:10.1016/j.epsl.2020.116164.

37. M. J. Cramwinckel, *et al.*, Global and Zonal-Mean Hydrological Response to Early Eocene Warmth. *Paleoceanography and Paleoclimatology* **38** (6), e2022PA004542 (2023), doi:10.1029/2022PA004542.

38. N. Thompson, *et al.*, Global Vegetation Zonation and Terrestrial Climate of the Warm Early Eocene. *Earth-Science Reviews* **261**, 105036 (2025), doi:10.1016/j.earscirev.2024.105036.

39. E. K. M. Chang, S. Lee, K. L. Swanson, Storm Track Dynamics. *Journal of Climate* **15** (16), 2163–2183 (2002), doi:10.1175/1520-0442(2002)015⟨02163:STD⟩2.0.CO;2.

40. P. A. O'Gorman, The Effective Static Stability Experienced by Eddies in a Moist Atmosphere. *Journal of the Atmospheric Sciences* **68** (1), 75–90 (2011), doi:10.1175/2010JAS3537.1.

41. T. Tamarin-Brodsky, Y. Kaspi, Enhanced Poleward Propagation of Storms under Climate Change. *Nature Geoscience* **10** (12), 908–913 (2017), doi:10.1038/s41561-017-0001-8.

42. H. Auestad, A. Shibu, P. Ceppi, T. Woollings, The Latent Heating Feedback on the Mid-Latitude Circulation. *Geophysical Research Letters* **52** (18), e2025GL116437 (2025), doi: 10.1029/2025GL116437.

43. V. Pope, R. Stratton, The Processes Governing Horizontal Resolution Sensitivity in a Climate Model. *Climate Dynamics* **19** (3), 211–236 (2002), doi:10.1007/s00382-001-0222-8.

44. E. Roeckner, *et al.*, Sensitivity of Simulated Climate to Horizontal and Vertical Resolution in the ECHAM5 Atmosphere Model. *Journal of Climate* **19** (16), 3771–3791 (2006), doi: 10.1175/JCLI3824.1.

45. J. Lu, *et al.*, Toward the Dynamical Convergence on the Jet Stream in Aquaplanet AGCMs. *Journal of Climate* **28** (17), 6763–6782 (2015), doi:10.1175/JCLI-D-14-00761.1.

46. J. Willison, W. A. Robinson, G. M. Lackmann, The Importance of Resolving Mesoscale Latent Heating in the North Atlantic Storm Track. *Journal of the Atmospheric Sciences* **70** (7), 2234–2250 (2013), doi:10.1175/JAS-D-12-0226.1.

47. R. C. J. Wills, A. R. Herrington, I. R. Simpson, D. S. Battisti, Resolving Weather Fronts Increases the Large-Scale Circulation Response to Gulf Stream SST Anomalies in Variable-Resolution CESM2 Simulations. *Journal of Advances in Modeling Earth Systems* **16** (7), e2023MS004123 (2024), doi:10.1029/2023MS004123.

48. P. R. Gent, J. C. Mcwilliams, Isopycnal Mixing in Ocean Circulation Models. *Journal of Physical Oceanography* **20** (1), 150–155 (1990), doi:10.1175/1520-0485(1990)020⟨0150:IMIOCM⟩2.0.CO;2.

49. P. R. Gent, The Gent–McWilliams Parameterization: 20/20 Hindsight. *Modelling and Understanding the Ocean Mesoscale and Submesoscale* **39** (1), 2–9 (2011), doi:10.1016/j.ocemod.2010.08.002.

50. I. Grooms, N. Agarwal, G. Marques, P. J. Pegion, H. Yassin, The Stochastic GM + E Closure: A Framework for Coupling Stochastic Backscatter With the Gent and McWilliams Parameterization. *Journal of Advances in Modeling Earth Systems* **17** (5), e2024MS004560 (2025), doi:10.1029/2024MS004560.

51. F. Castruccio, *et al.*, MESACLIP: A 10-Member Ensemble of CESM HR RCP 8.5 (2006-2100) Simulations (2024), doi:10.5065/PNCR-5S34.

52. F. Castruccio, *et al.*, MESACLIP: Nominal 1-Degree CESM (Low-Resolution) Simulations Corresponding to High-Resolution Experiments (2025), doi:10.5065/DBZQ-1K04.

53. G. Xu, *et al.*, High-Resolution Modelling Identifies the Bering Strait's Role in Amplified Arctic Warming. *Nature Climate Change* **14** (6), 615–622 (2024), doi:10.1038/s41558-024-02008-z.

54. J. W. B. Rae, *et al.*, Atmospheric CO2 over the Past 66 Million Years from Marine Archives. *Annual Review of Earth and Planetary Sciences* (2021), doi:10.1146/annurev-earth-082420-063026.

55. B. Hönisch, *et al.*, Toward a Cenozoic History of Atmospheric CO2. *Science* **382** (6675), eadi5177 (2023), doi:10.1126/science.adi5177.

56. G. A. Meehl, *et al.*, Effects of Model Resolution, Physics, and Coupling on Southern Hemisphere Storm Tracks in CESM1.3. *Geophysical Research Letters* **46** (21), 12408–12416 (2019), doi:10.1029/2019GL084057.

57. J. Zhu, *et al.*, Reduced ENSO Variability at the LGM Revealed by an Isotope-Enabled Earth System Model. *Geophysical Research Letters* **44** (13), 6984–6992 (2017), doi:10.1002/2017GL073406.

58. R. Knutti, D. Masson, A. Gettelman, Climate Model Genealogy: Generation CMIP5 and How We Got There. *Geophysical Research Letters* **40** (6), 1194–1199 (2013), doi:10.1002/grl.50256.

59. J. Zhu, C. J. Poulsen, B. L. Otto-Bliesner, High Climate Sensitivity in CMIP6 Model Not Supported by Paleoclimate. *Nature Climate Change* **10** (5), 378–379 (2020), doi:10.1038/s41558-020-0764-6.

60. M. Kageyama, *et al.*, The PMIP4 Last Glacial Maximum Experiments: Preliminary Results and Comparison with the PMIP3 Simulations. *Clim. Past* **17** (3), 1065–1089 (2021), doi:10.5194/cp-17-1065-2021.

61. J. M. Dennis, *et al.*, CAM-SE: A Scalable Spectral Element Dynamical Core for the Community Atmosphere Model. *The International Journal of High Performance Computing Applications* **26** (1), 74–89 (2011), doi:10.1177/1094342011428142.

62. F. Castruccio, Does Model Resolution Impact Its Climate Sensitivity? (2025).

63. N. Herold, *et al.*, A Suite of Early Eocene (˜ 55 Ma) Climate Model Boundary Conditions. *Geosci. Model Dev.* **7** (5), 2077–2090 (2014), doi:10.5194/gmd-7-2077-2014.

64. D. J. Lunt, *et al.*, Multi-Variate Factorisation of Numerical Simulations. *Geosci. Model Dev.* **14** (7), 4307–4317 (2021), doi:10.5194/gmd-14-4307-2021.

65. W. Rush, *et al.*, Assessing Environmental Change Associated with Early Eocene Hyperthermals in the Atlantic Coastal Plain, USA. *Clim. Past* **19** (8), 1677–1698 (2023), doi:10.5194/cp-19-1677-2023.

66. B. Schaefer, *et al.*, Paleoenvironmental Evolution during the Early Eocene Climate Optimum in the Chicxulub Impact Crater. *Earth and Planetary Science Letters* **589**, 117589 (2022), doi:10.1016/j.epsl.2022.117589.

67. A. Auderset, *et al.*, Enhanced Ocean Oxygenation during Cenozoic Warm Periods. *Nature* **609** (7925), 77–82 (2022), doi:10.1038/s41586-022-05017-0.

68. E. Anagnostou, *et al.*, Proxy Evidence for State-Dependence of Climate Sensitivity in the Eocene Greenhouse. *Nature Communications* **11** (1), 4436 (2020), doi:10.1038/s41467-020-17887-x.

69. J. S. Barnet, *et al.*, Coupled Evolution of Temperature and Carbonate Chemistry during the Paleocene–Eocene; New Trace Element Records from the Low Latitude Indian Ocean. *Earth and Planetary Science Letters* **545**, 116414 (2020), doi:10.1016/j.epsl.2020.116414.

70. E. Crouch, *et al.*, Climatic and Environmental Changes across the Early Eocene Climatic Optimum at Mid-Waipara River, Canterbury Basin, New Zealand. *Earth-Science Reviews* **200**, 102961 (2020), doi:10.1016/j.earscirev.2019.102961.

71. P. K. Bijl, *et al.*, Maastrichtian–Rupelian Paleoclimates in the Southwest Pacific – a Critical Re-Evaluation of Biomarker Paleothermometry and Dinoflagellate Cyst Paleoecology at Ocean Drilling Program Site 1172. *Clim. Past* **17** (6), 2393–2425 (2021), doi:10.5194/cp-17-2393-2021.

72. D. T. Harper, *et al.*, The Magnitude of Surface Ocean Acidification and Carbon Release During Eocene Thermal Maximum 2 (ETM-2) and the Paleocene-Eocene Thermal Maximum (PETM). *Paleoceanography and Paleoclimatology* **35** (2), e2019PA003699 (2020), doi:10.1029/2019PA003699.

73. D. T. Harper, *et al.*, Subtropical Sea-Surface Warming and Increased Salinity during Eocene Thermal Maximum 2. *Geology* **46** (2), 187–190 (2017).

74. S. B. Malevich, L. Vetter, J. E. Tierney, Global Core Top Calibration of δ18O in Planktic Foraminifera to Sea Surface Temperature. *Paleoceanography and Paleoclimatology* **34** (8), 1292–1315 (2019), doi:10.1029/2019PA003576.

75. J. E. Tierney, S. B. Malevich, W. Gray, L. Vetter, K. Thirumalai, Bayesian Calibration of the Mg/Ca Paleothermometer in Planktic Foraminifera. *Paleoceanography and Paleoclimatology* **34** (12), 2005–2030 (2019), doi:10.1029/2019PA003744.

76. J. E. Tierney, M. P. Tingley, A Bayesian, Spatially-Varying Calibration Model for the TEX86 Proxy. *Geochimica et Cosmochimica Acta* **127**, 83–106 (2014), doi:10.1016/j.gca.2013.11.026.

77. D. Evans, *et al.*, Eocene Greenhouse Climate Revealed by Coupled Clumped Isotope-Mg/Ca Thermometry. *Proceedings of the National Academy of Sciences* **115** (6), 1174–1179 (2018), doi:10.1073/pnas.1714744115.

78. C. K. West, *et al.*, Paleobotanical Proxies for Early Eocene Climates and Ecosystems in Northern North America from Middle to High Latitudes. *Clim. Past* **16** (4), 1387–1410 (2020), doi:10.5194/cp-16-1387-2020.

79. Z. Xiong, *et al.*, The Early Eocene Rise of the Gonjo Basin, SE Tibet: From Low Desert to High Forest. *Earth and Planetary Science Letters* **543**, 116312 (2020), doi:10.1016/j.epsl.2020.116312.

80. A. J. LOWE, *et al.*, DYNAMICS OF DEPOSITION AND FOSSIL PRESERVATION AT THE EARLY EOCENE OKANAGAN HIGHLANDS OF BRITISH COLUMBIA, CANADA: INSIGHTS FROM ORGANIC GEOCHEMISTRY. *PALAIOS* **37** (5), 185–200 (2022), doi:10.2110/palo.2021.007.

81. K. T. Smith, A. A. Bruch, Persistent Greenhouse Conditions in Eocene North America Point to Lower Climate Sensitivity. *Communications Earth & Environment* **6** (1), 352 (2025), doi:10.1038/s43247-025-02288-z.

82. N. Meijer, *et al.*, Proto-Monsoon Rainfall and Greening in Central Asia Due to Extreme Early Eocene Warmth. *Nature Geoscience* **17** (2), 158–164 (2024), doi:10.1038/s41561-023-01371-4.

83. M. Salpin, *et al.*, Evidence for Subtropical Warmth in the Canadian Arctic (Beaufort-Mackenzie, Northwest Territories, Canada) during the Early Eocene, in *Circum-Arctic Structural Events: Tectonic Evolution of the Arctic Margins and Trans-Arctic Links with Adjacent Orogens*, K. Piepjohn, J. V. Strauss, L. Reinhardt, W. C. McClelland, Eds. (Geological Society of America), vol. 541, p. 0 (2019), doi:10.1130/2018.2541(27).

84. D. A. Willard, *et al.*, Arctic Vegetation, Temperature, and Hydrology during Early Eocene Transient Global Warming Events. *Global and Planetary Change* **178**, 139–152 (2019), doi:10.1016/j.gloplacha.2019.04.012.

85. E. Dearing Crampton-Flood, J. E. Tierney, F. Peterse, F. M. Kirkels, J. S. Sinninghe Damsté, BayMBT: A Bayesian Calibration Model for Branched Glycerol Dialkyl Glycerol Tetraethers in Soils and Peats. *Geochimica et Cosmochimica Acta* **268**, 142–159 (2020), doi:10.1016/j.gca.2019.09.043.

86. R. D. Müller, *et al.*, The GPlates Portal: Cloud-Based Interactive 3D Visualization of Global Geophysical and Geological Data in a Web Browser. *PLOS ONE* **11** (3), e0150883 (2016), doi:10.1371/journal.pone.0150883.

87. K. J. Matthews, *et al.*, Global Plate Boundary Evolution and Kinematics since the Late Paleozoic. *Global and Planetary Change* **146**, 226–250 (2016), doi:10.1016/j.gloplacha.2016.10.002.

Acknowledgments

We acknowledge the National Science Foundation National Center for Atmospheric Research (NCAR) “Accelerated Scientific Discovery” program for providing computational resources on the Derecho system at the NCAR–Wyoming Supercomputing Center. We thank Jim Edwards for porting the model code to the new supercomputer and for his excellent technical support. We also thank Jesse Nusbaumer for assistance with the implementation of water isotopes, and Dave Hart and the staff of the Computational and Information Systems Laboratory (CISL) for their outstanding project support. D.J.L. thanks NCAR for providing an ‘Affiliate Scientist’ position.

Funding: J.Z. was funded by by National Science Foundation (NSF) grants 2303567 and 2202777. J.E.T., B.L.O., and J.Z. were funded by the Heising-Simons Foundation grant 2023-4716. The CESM project is supported primarily by the NSF. This material is based upon work supported by the National Center for Atmospheric Research (NCAR), which is a major facility sponsored by the NSF under Cooperative Agreement No. 1852977. We would like to acknowledge high-performance computing support from the Cheyenne (doi:10.5065/D6RX99HX) and Derecho (doi:10.5065/qx9a-pg09) systems provided by the NSF NCAR, sponsored by the NSF. D.B.B. was supported by the Cooperative Institute for Climate, Ocean, & Ecosystem Studies (CICOES) under

NOAA Cooperative Agreement NA20OAR4320271, Contribution No. 2026-1528.

Author contributions: J.Z. conceived the study, performed the simulations, conducted the analysis, and wrote the first draft of the manuscript. B.L.O., J.E.T., and J.Z. prepared the proposal for computational resource allocation. J.E.T. compiled the proxy temperature data and contributed to proxy analysis and interpretation of results. I.R.S. and D.B.B. contributed to the interpretation of the storminess analysis and the prescribed sea-surface temperature simulations. D.J.L. contributed to model-data comparison and interpretation of results. All authors contributed to the discussion of results and the revision of the manuscript.

Competing interests: There are no competing interests to declare.

Data and materials availability: The model code is available on GitHub (https://github.com/NCAR/iCESM1.3_iHESP_hires) and Zenodo (https://doi.org/10.5281/zenodo.18488808). Simulation data generated in this study will be made publicly through the Geoscience Data Exchange (GDEX) at the NSF NCAR (DOI to be added upon acceptance). Simulation data generated by the MESACLIP project are available through GDEX: low-resolution simulations (https://doi.org/10.5065/DBZQ-1K04) and high-resolution simulations (https://doi.org/10.5065/PNCR-5S34).

Supplementary materials

Materials and Methods
Figs. S1 to S6
References *(7-87)*
Data S1
Data S2

Supplementary Materials for

More equable past and future warm climates in unprecedented high-resolution simulations

Jiang Zhu*, Bette L. Otto-Bliesner, Jessica E. Tierney,
Esther C. Brady, Isla R. Simpson, David B. Bonan, Daniel J. Lunt
*Corresponding author. Email: jiangzhu@ucar.edu

This PDF file includes:

Materials and Methods
Figures S1 to S6
Captions for Data S1 to S2

Other Supplementary Materials for this manuscript:

Data S1 to S2

Materials and Methods

Model and Resolution

We use the Community Earth System Model version 1.3 with water isotope capabilities (CESM1.3) (*56, 57*). CESM1.3 retains the same model components as CESM1.2, including the Community Atmosphere Model version 5 (CAM5), the Community Land Model version 4 (CLM4), the Parallel Ocean Program version 2 (POP2), the Community Ice CodE version 4 (CICE4), and the River Transport Model (RTM). CESM1.3 incorporates additional bug fixes and performs comparably to CESM1.2 at the standard low-resolution (LR) configuration (∼1–2° for atmosphere/land and ∼1° for ocean/sea ice) (*56, 57*). Among Coupled Model Intercomparison Project phase 5 (CMIP5) models, the CESM1 family shows one of the closest matches to present-day observations across multiple performance metrics (*58*). It also reproduces large-scale temperature patterns across both glacial and greenhouse climates more accurately than other models including its CMIP6 successor (*6, 7, 9, 59, 60*).

In addition to the LR configuration, CESM1.3 includes infrastructure and code optimizations that enable high-resolution (HR) applications (*12, 13, 56*). The atmospheric component employs a spectral-element dynamical core that efficiently supports ~0.25° horizontal resolution (*61*), while the ocean and sea-ice components operate at ~0.1° resolution (*12*). All physical parameterizations remain identical to those in LR, except that oceanic mesoscale and submesoscale eddy parameterizations are disabled, as these processes are partially resolved at higher resolution. The HR model uses shorter timesteps to maintain numerical stability and includes minor retuning to achieve preindustrial radiation balance (*13*). In the modern climate, HR improves the simulation of mean conditions and extremes, including tropical cyclones, atmospheric rivers, and precipitation diurnal cycles, as well as coastal sea-surface temperatures (SSTs) (*12, 13*), while maintaining a comparable equilibrium climate sensitivity to LR (3.7 versus 3.6 °C in abrupt 4×CO_2 simulations) (*62*). Nevertheless, increased resolution does not uniformly improve performance: HR degrades some aspects, including both Arctic and Antarctic sea-ice extent, Antarctic Circumpolar Current transport, and ITCZ rainfall bias, and worsens ENSO frequency despite improving its amplitude (*13*).

Coupled simulations

The LR Eocene simulation is initialized from a previously published CESM1.2 experiment with identical boundary conditions, but using a finer ∼1° atmosphere–land grid instead of ~2° (*6, 20*). The boundary conditions include 3× preindustrial atmospheric CO_2 and non-CO_2 forcings (Eocene paleogeography and vegetation, absence of ice sheets and anthropogenic aerosols, and preindustrial orbital parameters) from the Deep-time Model Intercomparison Project (DeepMIP) (*7, 63*). The LR simulation is integrated for 300 years to allow the upper ocean to reach quasi-equilibrium under the altered atmospheric resolution. The resulting climatology closely resembles earlier CESM1.2 Eocene simulation that has been run for 2,200 years (not shown).

The high-resolution (HR) Eocene simulation is initialized using the ocean state at the end of the LR run. No discontinuities are observed in global mean surface temperature (GMST), and the top-of-model net radiation in the HR run adjusts rapidly, reaching values largely consistent with the differences seen between the PI HR and LR simulations (Figure S1). Boundary-condition fields are linearly interpolated from LR to HR, as higher-resolution fields such as paleogeography and vegetation distributions are unavailable. This approach maintains consistency between the two configurations and isolates the effects of model resolution. The HR simulation is integrated for 60 years due to its high computational cost—roughly 100 times that of the LR simulation. The HR configuration achieves an average throughput of one model year per day while producing high-frequency output suitable for weather analyses.

We also conduct hybrid-resolution simulations, in which the atmosphere and land components are run at high horizontal resolution while the ocean and sea ice remain at LR (High atmosphere Low ocean; HaLo). HaLo simulations are initialized from the ocean state from the corresponding LR and run for 60 and 50 years for the Eocene and PI, respectively (Figure S1). HaLo isolates the climatic impacts of atmospheric resolution from those associated with oceanic resolution. Specifically, comparing HaLo with LR quantifies the effect of high atmospheric resolution, while comparing HR with HaLo reveals contributions from higher oceanic resolution. This linear factorisation assumes that any nonlinearities (‘synergies’) between the atmospheric and oceanic resolution are small (*64*). In principle, an additional LaHo configuration (low-resolution atmosphere with high-resolution ocean) could further quantify these nonlinearities, but it is not pursued here due to the substantial effort required to retune the preindustrial simulation. Instead, we assess part of the potential nonlinearity using simpler atmosphere-only experiments (see section "Fixed SST simulations" below).

To assess the effects of model resolution on the climate response with a present-day continental configuration, corresponding abrupt-4×CO_2 simulations based on the preindustrial conditions are conducted. The LR 4×CO_2 simulation is integrated for 2,700 years to reach quasi-equilibrium. An HR 4×CO_2 simulation is then branched from the LR run, when the upper-ocean thermal state and large-scale circulation had equilibrated, and is integrated for 50 years (Figure S1).

We also analyze HR simulations under Representative Concentration Pathway 8.5 (RCP8.5) from the Understanding the Role of MESoscale Atmosphere-Ocean Interactions in Seasonal-to-Decadal CLImate Prediction (MESACLIP) project, which employ the same model configuration but exclude water isotopes. The MESACLIP preindustrial control is on average ~1.5 °C warmer in HR than LR, due to the limited tuning effort in their LR simulations (*13,19,51,52*). This differs from the PI simulation used in our study, which has been re-tuned via adjustment of the relative humidity threshold for low-cloud formation (rhminl) and thereby attains a GMST comparable to that of HR. Accordingly, when comparing RCP8.5 simulations between HR and LR, the LR fields are adjusted by the difference between the MESACLIP PI and our PI simulations (e.g., in Figure 6). Both LR and HR RCP8.5 ensembles consist of ten members each. We note that our HR PI simulation represents a 60-year extension of the 646-year MESACLIP HR PI run, augmented with water isotope capability.

Unless otherwise noted, the final 30 years of each simulation are used for analysis in this study, following the canonical definition of climate normal.

Fixed SST simulation

To further isolate the respective roles of atmospheric and oceanic resolution and to evaluate the role of SST-mediated atmospheric pathways, we perform a suite of low-resolution, atmosphere-only Eocene simulations forced with prescribed SSTs derived from the coupled HR (La_SST_{HR}), LR (La_SST_{LR}), and HaLo (La_SST_{HaLo}) experiments. These fixed-SST simulations are run for 30 years, with the last 25 years used for analysis. By comparing the atmosphere-only simulations with each other and with their coupled counterparts, we can quantify the impacts of resolution from complementary perspectives. For example, differences between La_SST_{HR} with La_SST_{LR}

isolates the effect of warmer SSTs associated with the high-resolution ocean in a low-resolution atmosphere, whereas contrasts between HaLo with $\mathrm{La\_SST_{HaLo}}$ isolates the effect of increased atmospheric resolution. Although additional high-resolution atmosphere-only simulations would further strengthen this separation and better capture potential nonlinear interactions, they were not conducted due to the high computational cost. Seasonal temperature responses from these simulations are shown in Figure 3, and additional analyses of storminess (not shown) are consistent with the interpretations presented in the main text.

Estimation of atmospheric and oceanic eddy activity

Daily 850-hPa zonal (u) and meridional (v) wind components are filtered using a 2–8-day Butterworth band-pass filter to isolate synoptic-scale variability. The eddy kinetic energy at 850 hPa ($\mathrm{EKE_{850}}$) is then computed as

$$\mathrm{EKE_{850}} = \frac{1}{2}\left(u'^2 + v'^2\right),$$

where primes denote band-pass-filtered anomalies. The resulting $\mathrm{EKE_{850}}$ fields are regridded to a common 1°×1° regular grid using linear interpolation prior to plotting. To improve the statistical robustness of the results, the analysis incorporates all winter days—December to February (DJF) in the Northern Hemisphere and June to August (JJA) in the Southern Hemisphere—rather than restricting the analysis to the coldest month. The results are shown in Figure 5 and are insensitive to the specific choices of filtering and regridding methods.

In addition to the high-frequency calculation described above, we estimate EKE from monthly mean model output to enable efficient diagnostics across multiple vertical levels and climate states. In this approach, EKE is approximated from the variance of monthly winds as

$$\mathrm{EKE} = \tfrac{1}{2}\left(\overline{u^2} + \overline{v^2} - \overline{u}^2 - \overline{v}^2\right),$$

where overbars denote monthly means. The terms $\overline{u^2}$ and $\overline{v^2}$ are provided directly by the model as the monthly means of squared velocities (UU and VV), while $\overline{u}$ and $\overline{v}$ are the monthly mean zonal and meridional winds (U and V). This formulation captures the submonthly wind variance within each month and therefore provides a first-order estimate of eddy kinetic energy. Although this approximation underestimates the absolute magnitude of EKE relative to calculations based on daily data, it does not affect the qualitative comparison among simulations and is therefore used for the vertical–latitudinal analysis shown in Figure S3.

Because high-frequency ocean data are unavailable, oceanic eddy activity is approximated from monthly mean sea surface height (SSH) and its square (SSH2). The standard deviation of SSH occurring on sub-month timescales (SSH_{SD}), serving as a coarse proxy for mesoscale variability, is estimated as

$$\mathrm{SSH_{SD}} = \left(\overline{\mathrm{SSH2}} - \overline{\mathrm{SSH}}^{2}\right)^{1/2},$$

where the overbars denote monthly averages from the available monthly model output.

Proxy Compilation

We compile sea-surface temperature (SST) proxies from the early Eocene Climate Optimum (EECO; 49.14–53.26 Ma) following the DeepMIP framework (*21*). In addition to the DeepMIP database, we incorporate recently published SST estimates from the Bass River (*24*), Knapps Narrows (*65*), M0077A (*66*), DSDP516 (*67*), IODPU1407, IODPU1409, and ODP1258 (*68*), IODPU1443 (*69*), Mid-Waipara River (*70*), ODP1172 (*71*), ODP1210 (*72*), and ODP1265 (*73*). The compilation includes SST estimates derived from foraminiferal δ^{18}O, Mg/Ca ratios, $\mathrm{TEX_{86}}$, and clumped isotopes, all processed using consistent calibration approaches (Supplementary Materials Data S1). For foraminiferal δ^{18}O–based temperatures, seawater isotope composition ($\delta^{18}\mathrm{O_{sw}}$) is obtained from the high-resolution simulation (this study) at the nearest model grid point, and pH effects are corrected following (*20*). The BAYFOX model is then used to convert the data to SST (*74*). Mg/Ca data are converted to SST using BAYMAG (*75*), assuming an Eocene ocean pH of 7.7 and carbonate saturation state (Ω) values drawn from a cGENIE Eocene simulation, consistent with the methodology in (*20*). $\mathrm{TEX_{86}}$-based estimates are derived using the BAYSPAR (Bayesian, spatially varying regression) calibration (*76*). For clumped isotope data, we use the temperatures given in ref. (*77*).

Mean annual air temperature (MAAT) and cold-month mean temperature (CMMT) estimates are compiled from the DeepMIP database (*21*) and previous syntheses (*4, 78*). We also include recently published records from the Gonjo Basin (*79*), McAbee (*80*), Oh!Locality (*81*), Xining Basin (*82*), Caribou Hills CaH2 (*83*), IODP302 (*84*), and Giraffe Kimberlite (*25, 26*). The terrestrial compilation (Supplementary Materials Data S2) uses the published values for MAAT and CMMT, with the exception of data from the MBT5Me proxy, which are recalibrated using the BAYMBT soils calibration (*85*).

All proxy sites are rotated to their 52 Ma paleogeographic positions following the DeepMIP protocol, using plate reconstructions and a hotspot-based rotation framework (*7, 63, 86, 87*).

Proxy records originating from the same location or from nearby sites (paleolatitude and paleolongitude differences $< 1^\circ$) are grouped together. Grouped estimates are combined using an uncertainty-weighted mean, with total uncertainties incorporating both analytical errors and the scatter among multiple proxy measurements. This grouping reduces the number of SST records from 40 to 29 and the number of terrestrial records from 100 to 53 (not all terrestrial sites contain both MAAT and CMMT; see the second tab in Supplementary Materials Data S1 and S2).

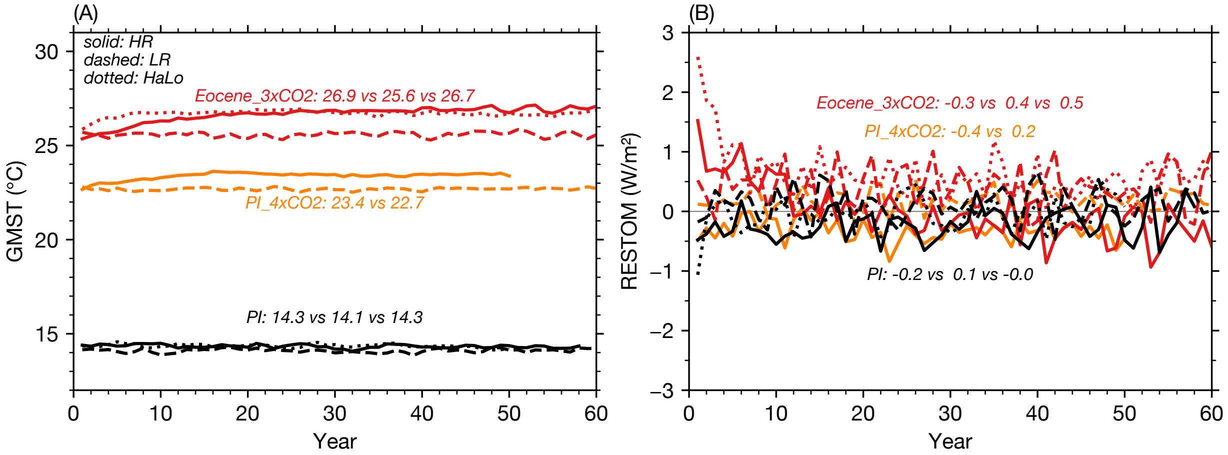

Figure S1: **Temporal evolution of global mean surface temperature and top-of-model net radiation.** (**A**) Annual mean global mean surface temperature (GMST) from all simulations: high resolution (HR), low resolution (LR), and hybrid configuration with a high-resolution atmosphere and low-resolution ocean (HaLo). (**B**) Annual mean top-of-model net radiation (RESTOM). Mean values over the final 30 years of each simulation are indicated in the panels. Note that the HR preindustrial simulation was an extension of an available spun-up run of 646 years (*13*)

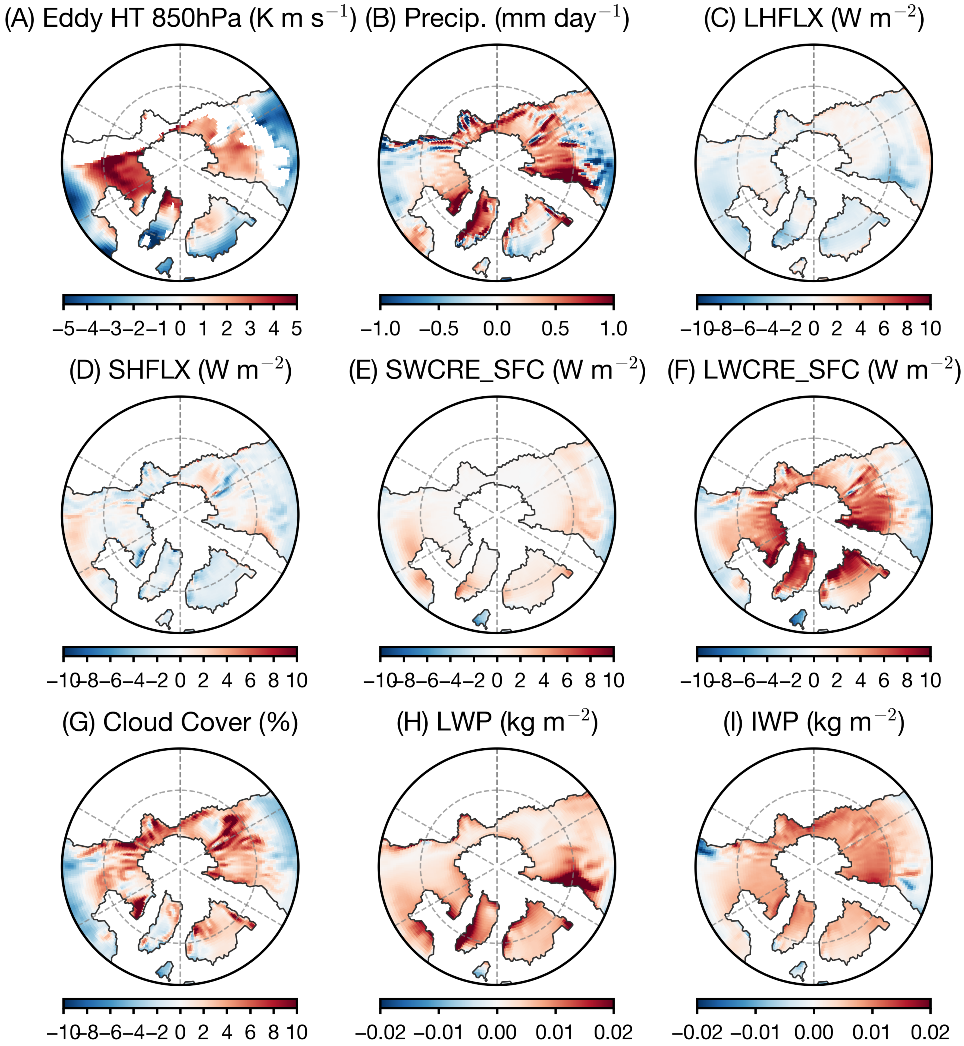

Figure S2: **Differences between the high-resolution (HR) and low-resolution (LR) Eocene simulations over the Northern Hemisphere high latitudes.** Panels show HR–LR differences in (**A**) Meridional heat transport by transient eddies at 850 hPa, (**B**) precipitation rate, (**C**) surface latent heat flux (LHFLX; positive downward leading to surface warming), (**D**) surface sensible heat flux (SHFLX; positive downward), (**E**) surface shortwave cloud radiative effect (SWCRE_SFC; positive downward), (**F**) surface longwave cloud radiative effect (LWCRE_SFC; positive downward), (**G**) total cloud cover in percentage, (**H**) cloud liquid water path (LWP), and (I) cloud ice water path (IWP). All fields are regridded to a common 1° grid prior to plotting. Relative to LR, the HR simulation exhibits enhanced precipitation and stronger LWCRE, accompanied by increased cloud fraction and cloud ice content.

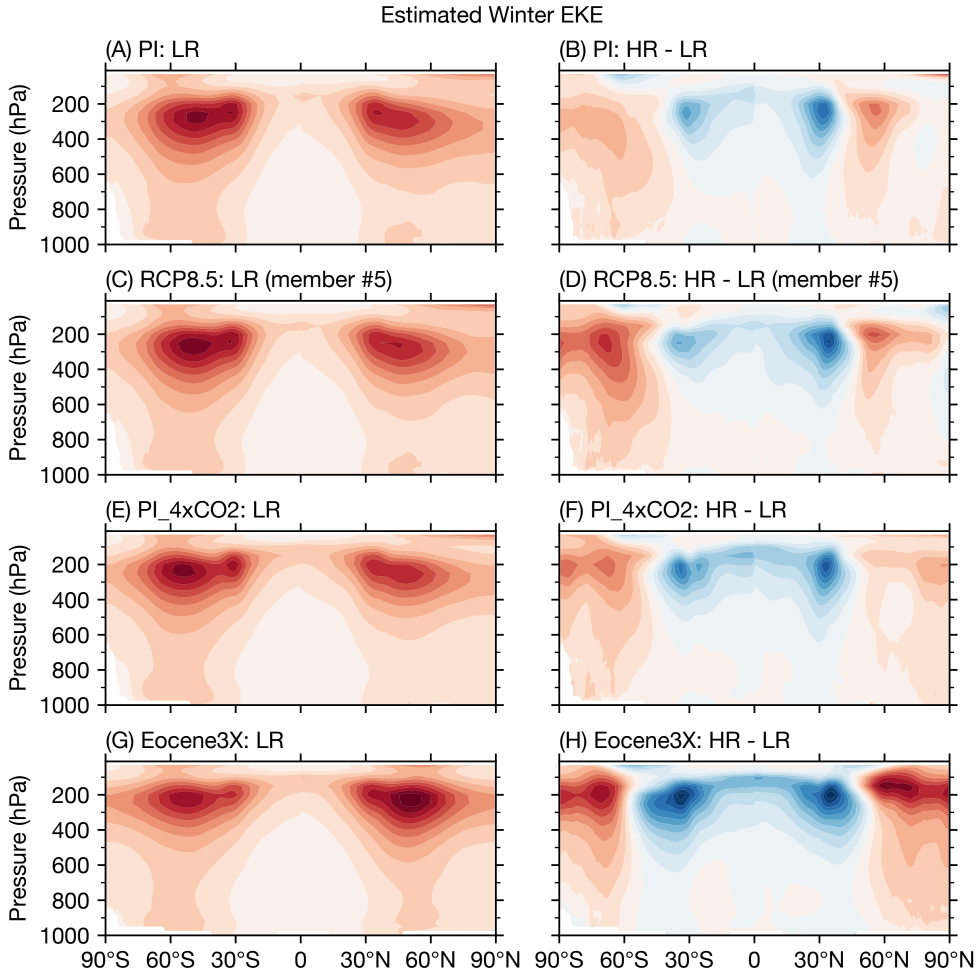

Figure S3: **High-resolution simulations enhance wintertime eddy kinetic energy (EKE) at high latitudes across climate states.** (**A, C, E, G**) Zonal-mean wintertime EKE from low-resolution (LR) simulations for preindustrial (PI), RCP8.5 (member #5), PI 4×CO_2, and Eocene 3×CO_2 climates, respectively. Panels (**B, D, F, H**) show the corresponding high-minus-low resolution (HR−LR) differences. For the RCP8.5 case, the HR−LR anomaly is corrected by subtracting the PI LR difference between this study and that from the MESACLIP to isolate the resolution-dependent response. MESACLIP RCP8.5 member #5 is shown; the signal is consistent across all 10 members.

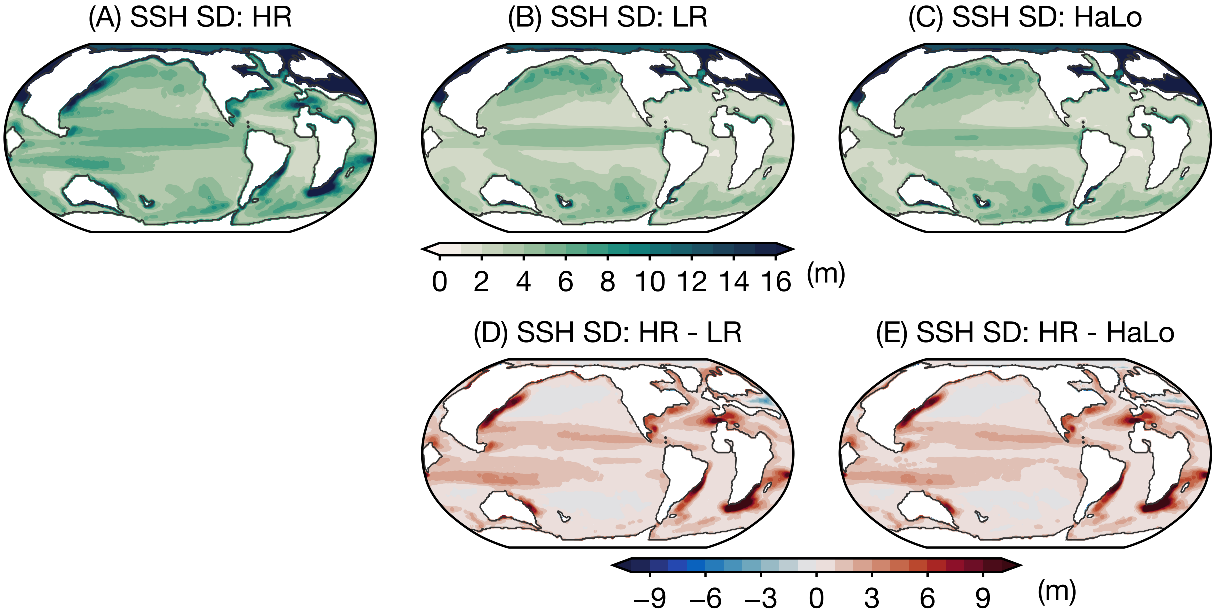

Figure S4: **Ocean eddy activity inferred from the standard deviation of sea surface height (SSH SD).** (**A**) SSH SD in the high-resolution (HR) Eocene simulation. (**B–C**) Same as **A**, but for the low-resolution (LR) and hybrid (HaLo; high-resolution atmosphere coupled to a low-resolution ocean) simulations. (**D, E**) Differences in SSH SD between the HR and HaLo simulations relative to LR, respectively.

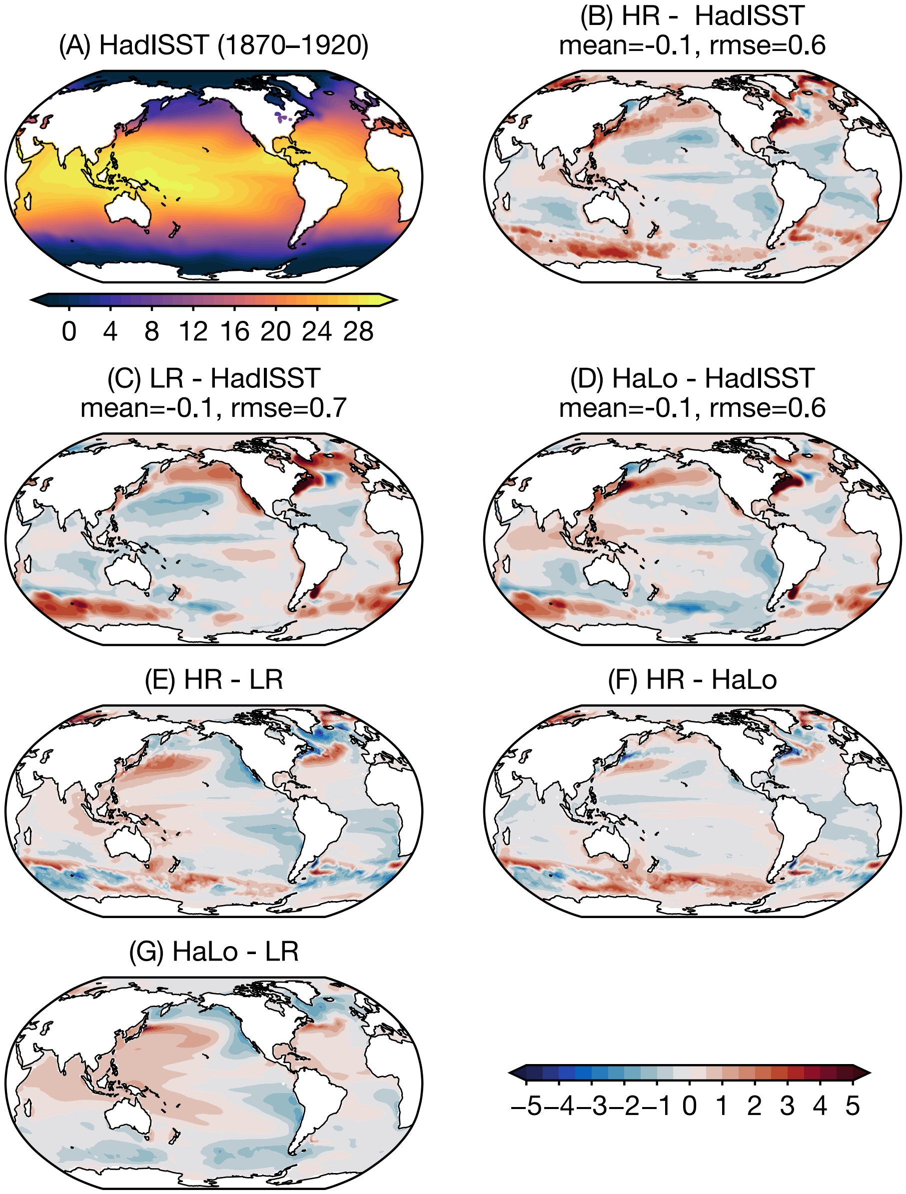

Figure S5: **High-resolution (HR) ocean simulations better capture SSTs in eddy-rich regions.** (**A**) Annual-mean sea-surface temperature (SST) from the HadISST dataset (1870–1920). (**B–D**) show SST differences between the low-resolution (LR), HR, and hybrid (HaLo; high-resolution atmosphere coupled to a low-resolution ocean) simulations and HadISST, respectively. (**E–G**) show pairwise SST differences among the HR, LR, and HaLo simulations, highlighting the ocean resolution-related SST improvements (e.g., **F** versus **D** and **C**), particularly in eddy-rich regions. Mean model bias and root-mean-squared error (RMSE) are indicated in the subfigure titles of **B–D**.

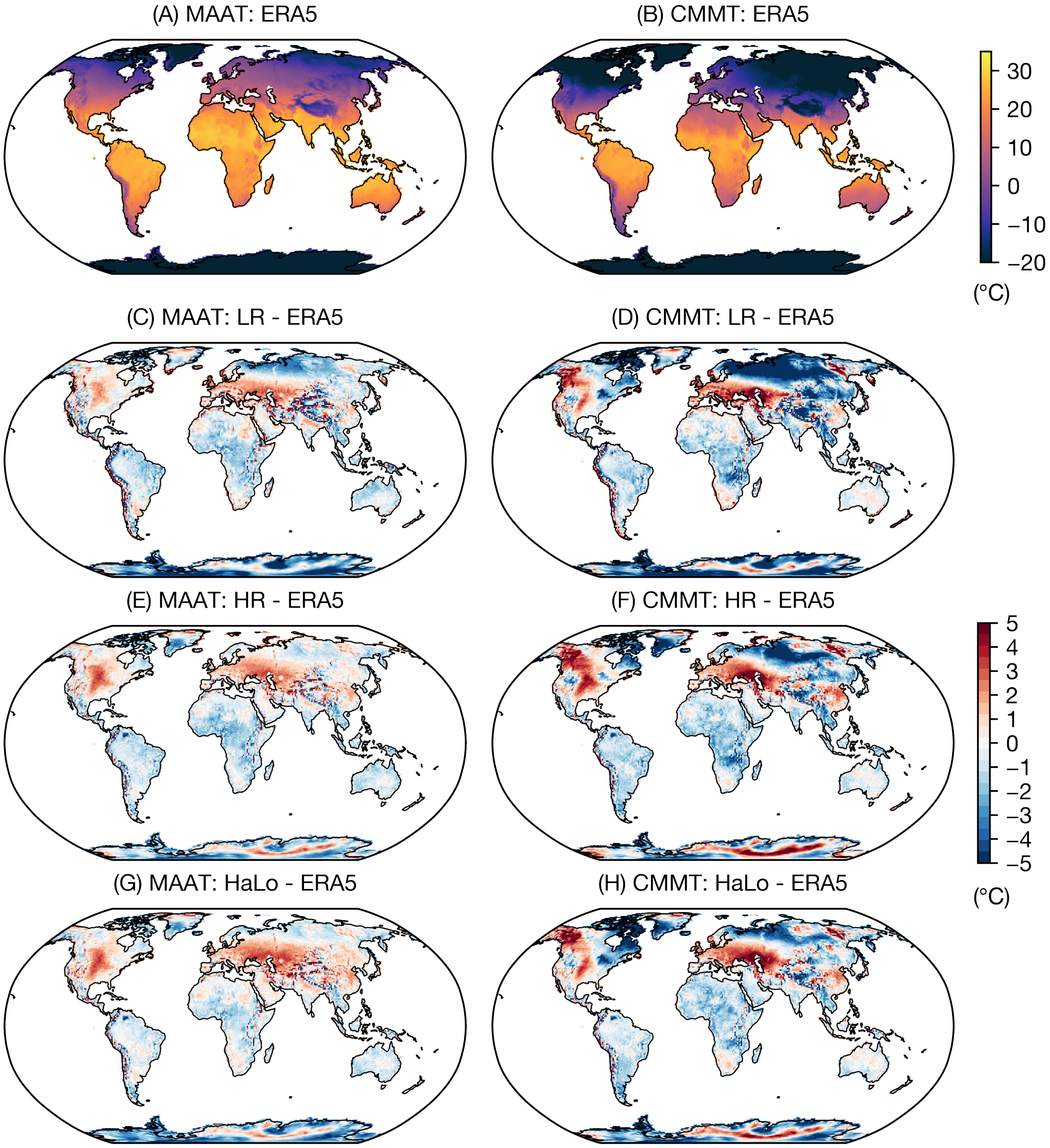

Figure S6: **High-resolution simulations better capture cold-month mean temperatures over high latitudes.** Mean annual surface air temperature (MAAT) (**A**) and cold-month mean temperature (CMMT) (**B**) from the ERA5 reanalysis (1950–1978). Panels (**C, D**) show differences in MAAT (C) and CMMT (D) between the low-resolution (LR) simulation and ERA5; (**E, F**) and (**G, H**) show the same for the high-resolution (HR) and hybrid simulations with a high-resolution atmosphere and low-resolution ocean (HaLo), respectively.

Caption for Data S1. Sea-surface temperature (SST) compilation for the early Eocene. Excel spreadsheet containing early Eocene marine SST reconstructions, including site name, age, modern coordinates, paleocoordinates, proxy type and proxy values, reconstructed SST estimates with associated 1σ uncertainties, and reference information.

Caption for Data S2. Terrestrial temperature compilation of the early Eocene: mean annual air temperature (MAAT) and cold-month mean temperature (CMMT). Excel spreadsheet containing early Eocene terrestrial temperature reconstructions, including site name, age, modern coordinates, paleocoordinates, proxy type and proxy values, reconstructed MAAT and CMMT with associated 1σ uncertainties, and reference information.